Determining electron–nucleus distances and Fermi contact couplings from ENDOR spectra†

Stephan Pribitzer, [ID] Donald Mannikko [ID] and Stefan Stoll [ID] *

The hyperfine coupling between an electron spin and a nuclear spin depends on the Fermi contact coupling a_{iso} and, through dipolar coupling, the distance r between the electron and the nucleus. It is measured with electron-nuclear double resonance (ENDOR) spectroscopy and provides insight into the electronic and spatial structure of paramagnetic centers. The analysis and interpretation of ENDOR spectra is commonly done by ordinary least-squares fitting. As this is an ill-posed, inverse mathematical problem, this is challenging, in particular for spectra that show features from several nuclei or where the hyperfine coupling parameters are distributed. We introduce a novel Tikhonov-type regularization approach that analyzes an experimental ENDOR spectrum in terms of a complete non-parametric distribution over r and a_{iso}. The approach uses a penalty function similar to the cross entropy between the fitted distribution and a Bayesian prior distribution that is derived from density functional theory calculations. Additionally, we show that smoothness regularization, commonly used for a similar purpose in double electron–electron resonance (DEER) spectroscopy, is not suited for ENDOR. We demonstrate that the novel approach is able to identify and quantitate ligand protons with electron–nucleus distances between 4 and 9 Å in a series of vanadyl porphyrin compounds.

1 Introduction

Hyperfine interactions, the magnetic couplings between unpaired electron spins and nearby nuclear spins, provide insight into the spatial distribution of the electron spin density and the geometric structure of paramagnetic spin centers. Hyperfine interactions are probed by high-resolution electron-nuclear double resonance (ENDOR) spectroscopy in solids[1] and solutions.[2,3] ENDOR directly measures nuclear resonance frequencies from which hyperfine couplings are extracted. Among the many pulse ENDOR techniques,[4] Davies ENDOR[5] and Mims ENDOR[6] are the two most common. ENDOR is extensively used, often in combination with isotope labeling, to determine the presence of magnetic nuclei near unpaired electron spins,[7–9] the extent of electron spin density delocalization,[10–13] and the distance and location of magnetic nuclei relative to an unpaired electron.[14–19] Electron–nucleus distances of up to 15 Å have been measured.[20]

The analysis of ENDOR spectra heavily relies on spectral simulation using ordinary least-squares fitting (LSQ) to fit a spin Hamiltonian model to the experimental spectrum. For spin-1/2 nuclei, the hyperfine parameters from this model uniquely

determine the ENDOR spectrum, which can be calculated from them in a straightforward fashion. The hyperfine interaction between an electron and a nucleus is represented by a hyperfine tensor that depends on up to six parameters: the isotropic Fermi contact coupling constant a_{iso}, the axial dipolar coupling constant T (which determines the effective distance r), the rhombicity η, and three parameters that describe the orientation of the tensor within the spin center. The number of parameters is reduced for nuclei distant from the electron spin density ($a_{iso} \approx 0$, $\eta \approx 0$) and in the case of non-orientation-selective ENDOR, where the three orientational parameters do not affect the ENDOR spectrum. The hyperfine coupling parameters contain information about the extent to which electron spin density is present at the nucleus, about the effective distance between the nucleus and the delocalized electron, and in orientation-selective situations, the location of the nucleus relative to the delocalized electron spin distribution.

Ordinary LSQ works reasonably well if the ENDOR spectrum contains non-overlapping features of only one or a few magnetic nuclei. It is more challenging for spin centers with many nuclei with overlapping ENDOR signatures and in the presence of substantial spread in the hyperfine couplings due to structural disorder (strain effects). In this case, extracting hyperfine parameters from the spectrum is a mathematically ill-posed problem in the sense that no unique solution exists, and that the solution is extremely sensitive to noise in the data.

Department of Chemistry, University of Washington, Seattle, WA 98195, USA.
E-mail: stst@uw.edu

A similar problem exists in double electron–electron resonance (DEER) spectroscopy. Like ENDOR, DEER probes magnetic dipolar couplings between pairs of spins, both electrons in this case. Experimental situations in DEER are usually such that contact couplings are negligible, the distances are relatively large, and orientation selection is absent. Therefore, the only coupling parameter that affects the dipolar spectrum is the effective inter-spin distance. In DEER, one common solution to the inversion problem of analyzing the data is Tikhonov regularization,[21] yielding a distribution of distances r between the two electrons.[22–25]

Here, we present a novel regularization-based method that analyzes an experimental ENDOR spectrum in terms of a complete non-parametric distribution over hyperfine parameters. We first show that ordinary LSQ fails, and that Tikhonov regularization, widely employed in DEER spectroscopy, is inadequate. We then introduce a regularization approach that augments the LSQ objective function with a penalty term that measures the dissimilarity between the distribution and a prior probability distribution that is obtained from computational-chemistry predictions. This term penalizes regions in hyperfine parameter space that are deemed nonphysical for the molecules under investigation, based on the calculations. We demonstrate and evaluate the method on non-orientation-selective ligand ^{1}H ENDOR spectra of a series of vanadyl porphyrin compounds. These pose a particularly challenging problem, as they have a large number of protons with strongly overlapping ENDOR spectra, as well as protons with significant distributions of hyperfine parameters.

2 The ENDOR spectrum

ENDOR provides a spectrum of nuclear resonance frequencies ν_n of the spin center. For a spin-1/2 nucleus interacting with a spin-1/2 electron with an isotropic g value, they are[26]

$$\nu_n(m_S) = \|(\nu_I \mathbf{1} + m_S \boldsymbol{A})\boldsymbol{z}_L\| \qquad (1)$$

where $m_S = \pm 1/2$, $\|\ldots\|$ indicates the Euclidean norm, $\boldsymbol{z}_L$ is the unit vector along the applied laboratory magnetic field $\boldsymbol{B}_0$, $\mathbf{1}$ is the 3×3 identity matrix, and $\nu_I = -g_n\mu_N B_0/h$ is the nuclear Larmor frequency, with the nuclear g factor g_n, the nuclear Bohr magneton μ_N, the applied magnetic field magnitude $\boldsymbol{B}_0$, and the Planck constant h.

$\boldsymbol{A}$ is the molecule-fixed hyperfine coupling tensor, in frequency units. It is a 3×3 matrix consisting of a sum of two main physical contributions

$$\boldsymbol{A} = a_{iso}\mathbf{1} + \boldsymbol{A}_{dip} \qquad (2)$$

The first term is the isotropic Fermi contact coupling constant

$$a_{iso} = \frac{8\pi}{3}\frac{\mu_0}{4\pi}\frac{\mu_N g_n \mu_B g_e}{h}\rho(\boldsymbol{R}) \qquad (3)$$

Here, μ_0 is the magnetic constant, μ_B the Bohr magneton, g_e is the electron g value, and $\rho(\boldsymbol{R})$ is the (positive or negative) electron spin density at $\boldsymbol{R}$, the location of the nucleus. This term captures the interaction between the nucleus and the

electron spin density at its position. The second term in eqn (2) is the dipolar coupling tensor, with elements

$$(\boldsymbol{A}_{dip})_{ij} = \frac{\mu_0}{4\pi}\frac{\mu_N g_n \mu_B g_e}{h}\int \rho(\boldsymbol{r})\frac{3n_i n_j - \delta_{ij}}{\|\boldsymbol{r} - \boldsymbol{R}\|^3}d\boldsymbol{r} \qquad (4)$$

where $i, j = x, y, z$, $\boldsymbol{r}$ is the electron location, n_i and n_j are components of the unit vector $\boldsymbol{n} = (\boldsymbol{r} - R)/\|\boldsymbol{r} - \boldsymbol{R}\|$ along the nucleus-electron direction, and δ_{ij} is the Kronecker delta. This term captures the anisotropic through-space magnetic dipolar coupling of the nucleus with the electron averaged over the electron spin density distribution. Note the inverse-cube dependence on the electron–nucleus distance.

In its principal-axis system, the dipolar tensor is diagonal, and the hyperfine tensor is

$$\boldsymbol{A} = \begin{pmatrix} a_{iso} - T(1 - \eta) & 0 & 0 \\ 0 & a_{iso} - T(1 + \eta) & 0 \\ 0 & 0 & a_{iso} + 2T \end{pmatrix} \qquad (5)$$

where the dipolar coupling constant T describes the strength of the dipolar interaction and the rhombicity parameter $0 \leq \eta \leq 1$ quantifies the deviation of $\rho(\boldsymbol{r})$ from cylindrical symmetry around the $\boldsymbol{n}$ axis.

In this work, we mostly restrict ourselves to the situation where the nucleus and the electron spin density distribution are far enough apart such that the point-dipole approximation holds, i.e. the electron–nucleus distance is much larger than the spread of the spin density. In this case, rhombicity is negligible ($\eta \approx 0$), and T becomes

$$T = \frac{\mu_0}{4\pi}\frac{\mu_N g_n \mu_B g_e}{h}\frac{1}{r^3} \qquad (6)$$

where r is the effective distance between nucleus and electron.

Through eqn (1), the ENDOR spectrum depends on the orientation of the spin center relative to the applied field. The ENDOR spectrum for a powder or frozen-solution sample with a uniform distribution of spin center orientations is the integral of these spectra over all orientations of the spin center. The shape and width of the resulting "powder" spectrum strongly depend on a_{iso} and T.

When using Mims ENDOR to measure the ENDOR spectrum, spectral intensities are subject to a frequency-dependent suppression that depends on τ, the delay between the first two pulses in the Mims ENDOR pulse sequence.[28] It results in blind spots, i.e. frequencies of maximal suppression, at $\nu_I \pm n/2\tau$, where $n = 0, 1, 2,\ldots$. This suppression effect is illustrated in Fig. 1a. The Mims ENDOR spectra (color) are overlaid on the unsuppressed ENDOR spectra (dashed, gray lines). The hyperfine parameters used for the simulations are shown in Fig. 1b. The suppression effect has a significant impact on the shape of the ENDOR spectrum; narrow spectra in particular end up resembling pairs of Gaussians due to the central blind spot at $\nu = \nu_I$ ($n = 0$; the 'hole in the middle'[29]).

Besides magnetic nuclei that are part of the spin center, ENDOR also reveals interactions with nuclei from the solvent matrix and from other spin centers. These nuclei are spatially
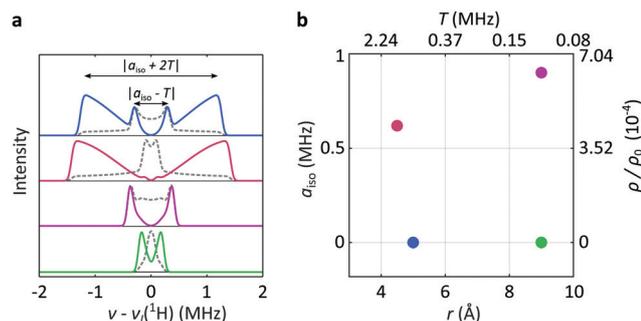
This journal is © the Owner Societies 2021

Phys. Chem. Chem. Phys., 2021, **23**, 8326–8335 | **8327**

Fig. 1 (a) Simulated powder Mims ENDOR spectra (colored) of protons with typical axial hyperfine tensors, with τ = 150 ns, together with simulated spectra without τ suppression (gray). The shape and the width of the spectrum depend on a_{iso} and T. Spectra are centered around the nuclear Larmor frequency of the proton $\nu_I(^1H)$, were simulated at 344 MHz, and are scaled to maximum 1. (b) Hyperfine parameters used for the spectra in (a), in addition to $\eta = 0$. The top and bottom horizontal axes show the dipolar coupling constant T and the associated effective electron–nucleus distance r. The vertical axes show a_{iso} and the associated contact electron spin density $\rho(\mathbf{R})$, expressed as a fraction in relation to the contact spin density in a hydrogen atom, ρ_0, corresponding to $a_{iso,0}$ = 1420 Mhz.[27]

uniformly distributed and lead to a narrow peak in the ENDOR spectrum centered at the Larmor frequency that can have significant intensity despite the τ-dependent suppression. The appearance of this matrix peak has been studied in detail,[30,31] and an excluded-volume model similar to one used in DEER can be applied.[32] Since all data in this paper were acquired at low concentrations in fully deuterated solvents, the overall proton density is low. Therefore, we model the matrix peak as a Lorentzian

$$L(\nu) = \frac{1}{\pi} \frac{\delta/2}{(\nu - \nu_I(^1H))^2 - (\delta/2)^2} \tag{7}$$

were δ describes the width of the Lorentzian. Other choices of matrix line shapes are possible.

3 Model compounds

We demonstrate our method with the four uncoordinated vanadyl porphyrin compounds shown in Fig. 2a. They all have an identical porphin core with close protons (pyrrole and meso), and differ in the substitution patterns that provide a large number of distant protons. We investigate the effect of meso substituents on the ENDOR spectrum by using vanadyl tetraphenylporphyrin (VO-TPP; no meso protons) and vanadyl diphenylporphyrin (VO-DPP; two meso protons). In vanadyl octaethylporphyrin (VO-OEP) and vanadyl etioporphyrin (VO-EP), the pyrrole protons are all substituted with ethyl groups (VO-OEP) or a mix of methyl and ethyl groups (VO-EP), but the protons at the four meso positions are preserved. The large number of protons with similar small hyperfine couplings makes it particularly challenging to analyze the associated ENDOR spectra.

We use density functional theory (DFT) calculations to predict all ^1H hyperfine tensors for all five complexes in Fig. 2a. The results are shown in Fig. 2b. Different types of protons appear in distinct regions of the (r,a_{iso}) plane. Protons directly attached to the tetrapyrrole ring (meso and pyrrole) have non-negligible and positive a_{iso}. In contrast, all protons from aliphatic and aromatic substituents and from the THF ligand have a_{iso} values close to zero, but of either sign. The DFT calculations also predict that all proton hyperfine tensors are essentially axial, with $\eta \approx 0.07$ for the meso protons and $\eta < 0.04$ for all others (data not shown). The distinction between protons from THF and *ortho* protons from VO-TPP and VO-DPP is difficult, as both have a_{iso} close to zero and r in the range of about 5 Å. In general, distant protons from larger axial ligands and closer protons on ring substituents are not distinguishable based on a_{iso} and r alone.

4 Ordinary least-squares analysis

The calculation of the ENDOR spectrum $S(\nu)$ for a given hyperfine parameter distribution $P(r,a_{iso})$ is straightforward:
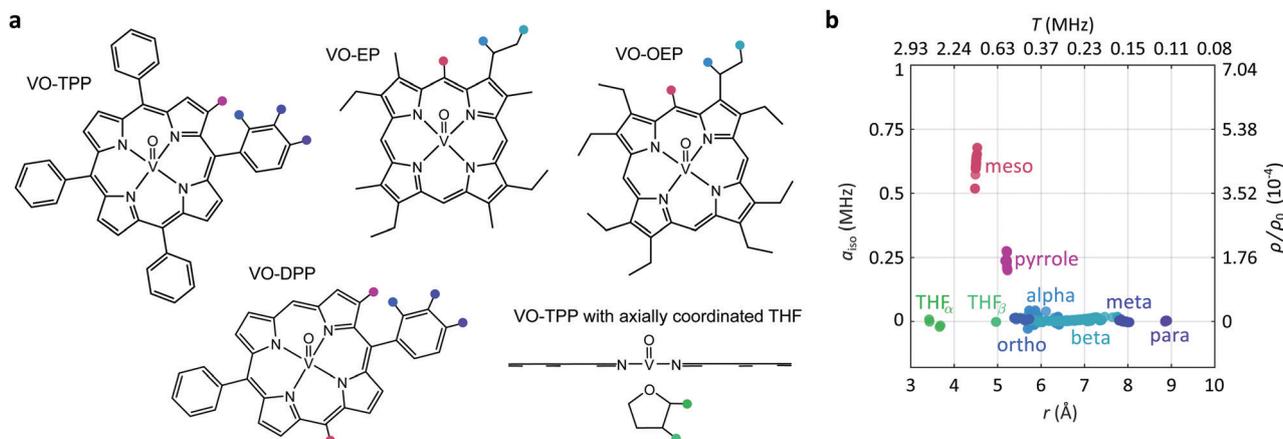
$$S = KP \tag{8}$$

Fig. 2 (a) Lewis structures of the four model compounds examined in this study, plus VO-TPP axially coordinated by tetrahydrofuran (THF). The different types of protons are indicated in color. (b) Hyperfine coupling parameters determined from DFT calculations for protons from all structures.

8328 | *Phys. Chem. Chem. Phys.*, 2021, **23**, 8326–8335

This journal is © the Owner Societies 2021

Here, S is the ENDOR spectrum in vector form, and P is the vector form of a histogram representation of $P(r,a_{iso})$ discretized over a sufficiently fine grid of r and a_{iso}, i.e. $P_i = P(r_i,a_{iso,i})$. K is a kernel matrix where column i contains the simulated ENDOR spectrum for the parameter combination $(r_i,a_{iso,i})$. These spectra form the basis functions of the problem. To model the matrix peak, one column is added to K that contains the Lorentzian line from eqn (7), and the P vector is augmented by one element to provide the amplitude of the matrix peak basis function.

Inverting eqn (8) consists of estimating P from the measured spectrum S. One possible approach is to use ordinary least-squares fitting

$$P_{fit} = \arg\min_{P \geq 0} ||S - KP||^2 \qquad (9)$$

where $P \geq 0$ indicates that all values in the distribution vector must be nonnegative. This constitutes a mathematically ill-posed problem, since the condition number of K is very large (on the order of 10^{18} in our case). In other words, the set of ENDOR basis spectra in K have very similar shapes and are almost linearly dependent. This is illustrated in Fig. 3, which shows that a spectrum from a proton with medium r and small a_{iso} can be fit by a proton with long r and a wide distribution of a_{iso}. This means small changes in the spectrum (such as noise) can lead to large changes in the fitted distribution, and a measured noisy spectrum may be fit equally well by several different P.

Fig. 4a top shows the experimental spectrum of VO-TPP in red and the fitted spectrum obtained using eqn (9) in blue, together with the residual vector. The bottom panel shows the fitted $P(r,a_{iso})$ as well as its projections onto the r and a_{iso} dimensions. For reference, the results of the DFT calculations from Fig. 2 are shown as gray circles. The fit to the spectrum is excellent, with the residuals not displaying any noticeable systematic deviations. However, the fitted $P(r,a_{iso})$ strongly deviates from the physical predictions obtained from DFT.
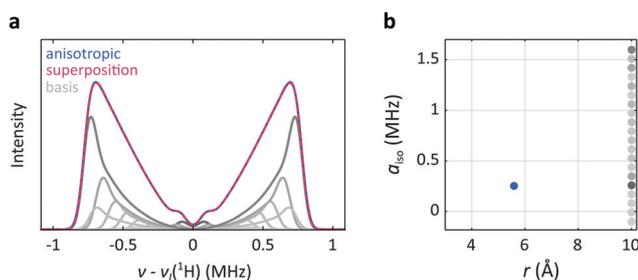

Fig. 3 Demonstration of linear dependence within the basis set of Mims ENDOR spectra. (a) An anisotropic spectrum (a_{iso} = 0.62 MHz, T = 0.64 MHz), simulated at B_0 = 350 mT, is fit accurately by a linear combination of basis spectra with a small dipolar contribution and large variation in contact coupling (a_{iso} = −0.1–1.6 MHz, T = 0.079 MHz). The resulting superposition (red) reproduces the anisotropic spectrum almost perfectly. The combinations or r and a_{iso} are shown in (b). Color saturation of the dots for the basis spectra indicates relative weights in the linear combination.

Clearly, the LSQ approach is unsatisfactory. This is a consequence of the severe ill-posedness of the problem. Additional information must be included in the analysis to obtain a unique and stable solution.

5 Regularized least-squares analysis

To include additional information, we use Tikhonov regularization.[21] This is a well-established method that augments the objective function with a P-dependent quadratic penalty term:

$$P_{fit} = \arg\min_{P \geq 0}\left(||S - KP||^2 + \alpha^2||\Gamma P||^2\right) \qquad (10)$$

with a regularization operator Γ and a regularization parameter α. This second term helps to stabilize the solution. Various choices for the regularization operator Γ exist: the identity operator minimizes the amplitude of each basis function and avoids spikes in the target distribution. The first and second differential operators can be good choices if the probability distributions are expected to be smooth. Other operators are possible as well.

The regularization parameter α controls the balance between data agreement and regularization; a large value for α prioritizes the regularization and will tolerate a discrepancy between fit and data. What exactly constitutes a large or small value for α depends on the number of data points, the scale of the spectrum, and the regularization operator. Various approaches exist for the selection of an α value, based on various conceptions of optimality.[33] To select appropriate regularization parameters, we used the Akaike information criterion (AIC).[34] For DEER spectroscopy, AIC has been shown to be one of the most reliable selection methods.[33]

The second term in eqn (10) represents additional information, and from a Bayesian perspective, it represents a prior, i.e. information about the spin center that is available prior to taking the ENDOR spectrum into account.

We examine two choices for Γ. First, we utilize the second derivative, corresponding to a smoothness prior, and show that it does not work. Then, we introduce an operator that calculates the dissimilarity to a physically expected distribution, obtained from structure-based DFT calculations.

5.1 Smoothness regularization

We first examine the use of the second derivative for the regularization operator Γ in eqn (10). This choice is very common in DEER spectroscopy.[22–25] There, a one-dimensional distance distribution $P(r)$ is fitted to the experimental signal. In contrast, in our case the target distribution $P(r,a_{iso})$ is two-dimensional. We therefore include separate regularization terms along the r dimension and the a_{iso} dimensions:

$$
\begin{aligned}
P_{fit} &= \arg\min_{P \geq 0}\left(||S - KP||^2 + \alpha_r^2||\Gamma_r P||^2 + \alpha_a^2||\Gamma_a P||^2\right) \\
&= \arg\min_{P \geq 0}\left(||S - KP||^2 + \left|\left|\begin{pmatrix}\alpha_r\Gamma_r \\ \alpha_a\Gamma_a\end{pmatrix}P\right|\right|^2\right)
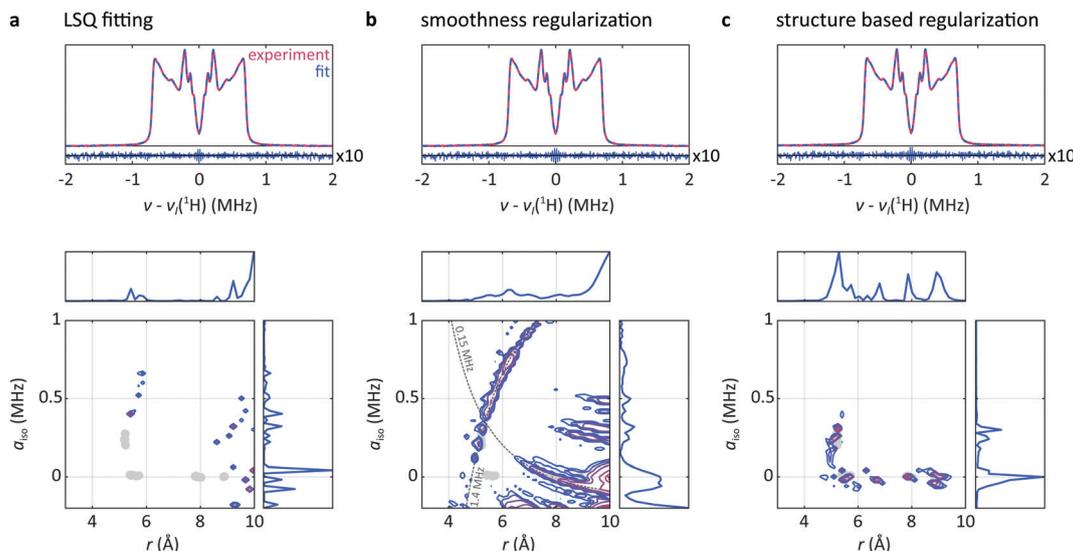\end{aligned} \qquad (11)
$$

Fig. 4 (a) The solution for the ordinary least square fitting approach for VO-TPP, eqn (9). (b) The same data analyzed with smoothness regularization as shown in eqn (11). (c) Regularization with penalty function based on the $\tilde{P}$ shown in Fig. 5 and using eqn (12). For (b) and (c) the regularization parameters were selected *via* the AIC method. The top panels show the experimental spectrum in red and the fit to it in blue, as well as the residuals with a magnification factor of 10. The bottom panels show the density distribution over distance r and contact coupling a_{iso} that was fit to the spectrum, with contour levels at 0.02, 0.05, 0.1, 0.2, 0.5, 0.75, and 0.9 of the distribution maximum. The DFT results for the protons in VO-TPP (pyrrole, *ortho*, *meta*, and *para*) are shown as gray dots. The dotted lines in the lower panel of (b) indicate locations of constant $|a_{iso} + 2T| \approx 1.4$ MHz and of constant $|a_{iso} - T| \approx 0.15$ MHz.

Here, Γ_r and Γ_a are matrices representing the second derivative along a_{iso} and r, respectively, and α_a and α_r are the associated independently selectable regularization parameters.

An analysis of the ENDOR spectrum of VO-TPP using this approach, combined with AIC for the selection of both regularization parameters, is shown in Fig. 4b. The fit to the spectrum is excellent, as in the case of ordinary LSQ. However, the fitted distribution is starkly different. There is significant density at nonphysical combinations of long r and large a_{iso}, inconsistent with the expectations from the DFT calculations (Fig. 2b). Also, the fitted distribution in Fig. 4b shows extended ridges. The more vertical ridge runs along locations of constant $|a_{iso} + 2T| \approx$ 1.4 MHz and corresponds to a set of spectra with equal overall width (see Fig. 1a). Peaks at some locations along this ridge are also visible in the LSQ fit. The more horizontal ridge runs along locations of constant $|a_{iso} - T| \approx 0.15$ MHz. The associated set of spectra have identical locations of their inner peaks (see Fig. 1a). Both ridges are a consequence of the smoothness requirement imposed by the second term in eqn (11). Varying α_r and α_a or using the identity or the first derivative as regularization operators does not improve the situation.

The reason this approach fails is that the added requirement of smoothness along the r and a_{iso} dimensions is not entirely physical. While it might be reasonable to expect some distribution of a_{iso} for the meso protons as a result of structural flexibility of the molecule, the distribution of a_{iso} for more distant protons is expected to be much narrower. Imposing a uniform smoothness requirement over the entire range of a_{iso} is therefore not representative of the physical expectation. A similar argument holds for distributions along the r

dimension, where different nuclei will have vastly different distributions of r, depending on the local structural flexibility in the molecule.

5.2 Structure-based regularization

Since we have information from DFT that enables us to distinguish physical from nonphysical solutions, it is advantageous to incorporate this information directly and quantitatively into the objective function. To do this, we solve the regularized minimization problem

$$P_{\text{fit}} = \underset{P \geq 0}{\arg\min} \left(||S - KP||^2 + \alpha_P^2 ||\Gamma_P P||^2 \right) \quad (12)$$

with a regularization operator Γ_P that penalizes P in (r, a_{iso}) regions that are deemed non-realistic based on structural information from quantum-chemical calculations. One form of Γ_P that achieves this is the multiplicative operator

$$\Gamma_P = -\ln \tilde{P} \quad (13)$$

where $\tilde{P}$ is a probability distribution over r and a_{iso} that captures physical expectations about $P(r, a_{iso})$. Unphysical regions in the (r, a_{iso}) domain have small values of $\tilde{P}$ and therefore large values of Γ_P, and increase the value of the objective function. With this operator, the discretized form of the norm in the regularization term in eqn (12) is

$$||\Gamma_P P||^2 = \sum_i [(-\ln \tilde{P}_i) P_i]^2 \quad (14)$$

This is similar to the cross entropy[35–37] of $\tilde{P}$ relative to P, $\sum_i (-\ln \tilde{P}_i) P_i$. Although it is possible to use the cross entropy
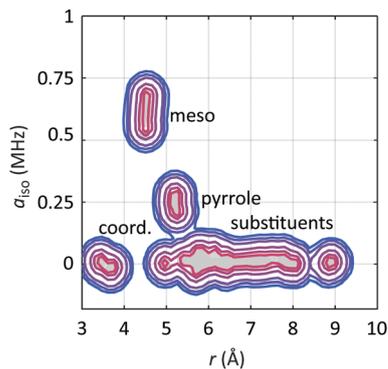
Fig. 5 The probability distribution $\tilde{P}$, overlaid on the results from the DFT calculations (gray). Contour levels are at 0.05, 0.1, 0.2, 0.5, 0.75, and 0.9 of the distribution maximum.

directly as a regularization term, we utilize the squared form to keep the objective function of the general quadratic form in eqn (10).

The distribution $\tilde{P}$ for the application case in this paper is shown in Fig. 5. It is constructed using the results from the DFT calculations shown in Fig. 2. Mathematical details are given in the Methods section below. It is designed to have significant amplitude at and near locations of DFT predictions, and very small but non-zero amplitude everywhere else, thereby representing our expectation about P. Significant broadening is added to represent uncertainty that accounts for potential errors in the DFT calculations or the underlying structures. One possible alternative to this structure-based $\tilde{P}$ is to completely exclude basis functions from the kernel that lie in physically unrealistic regions, equivalent to setting $\tilde{P}$ to zero in these regions. In principle, excluding basis functions could also be applied to the LSQ and smoothness approaches, which is just

another way of incorporating additional information. However, a $\tilde{P}$ that is non-zero everywhere has a crucial advantage, as it does not categorically exclude any (r, a_{iso}) region from being included in the fit. With $\tilde{P}$ as defined, the method is able to identify protons with large r and a_{iso} if there is strong evidence for them in the data. In general, it is important to keep $\tilde{P}$ diffuse enough not to categorically exclude any region.

The result of analyzing the VO-TPP spectrum using eqn (12) with AIC-selected regularization parameter α_P is shown in Fig. 4c. The fit to the data is as excellent as with the other methods. The fact that all three methods result in excellent fits to the spectra that are more or less identical despite gross differences among the fitted distributions illustrates the strong ill-posedness of the problem and the importance of including additional information *via* regularization. Importantly, however, now the fitted distribution is more physical: it contains very little intensity outside the expected regions, and extended ridges are absent.

As in any regularization approach, the selection of a value for α_P plays an important role. If α_P is chosen too small, the effect of regularization is reduced, leading to density in areas of nonphysical (r, a_{iso}). On the other hand, large values of α_P lead to P_{fit} with very narrow spikes at some of the maxima of the prior probability function $\tilde{P}$.

6 Results for all compounds

The results for the analysis of all four model compounds are shown in Fig. 6. All ENDOR spectra are fitted very accurately, with all residual vectors showing no significant systematic deviations from zero. All fitted hyperfine distributions are physically reasonable. The method recovers the expected hyperfine
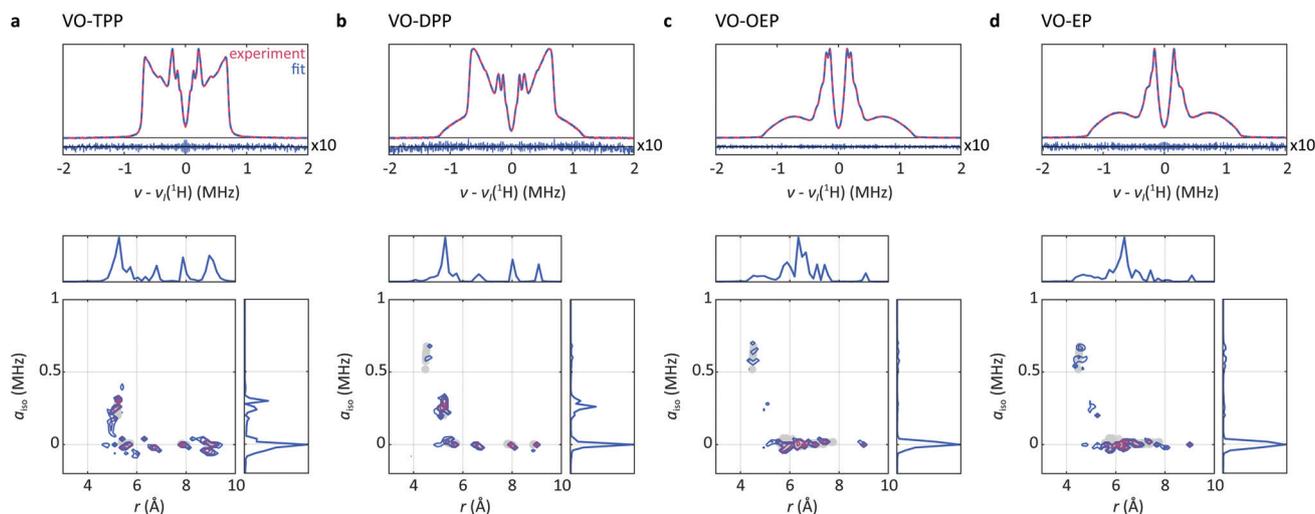

Fig. 6 Analysis of the four model vanadyl porphyrin compounds, (a) VO–TPP, (b) VO–DPP, (c) VO–OEP, and (d) VO–EP. The top panels show the experimental spectrum in red and the fit to it in blue, as well as the residuals with a magnification factor of 10. The bottom panels show the distance r vs. contact coupling a_{iso} distribution that was fit to the spectrum, with contour levels at 0.02, 0.05, 0.1, 0.2, 0.5, 0.75, and 0.9 of the distribution maximum, as well as its projections along a_{iso} and r. Results from the DFT simulations for protons of the same type as in the individual compounds are shown as gray dots.

couplings well for all investigated compounds: it correctly determines that meso protons are absent in VO-TPP and present in all other complexes, and that there are no pyrrole protons in VO-OEP and VO-EP, in contrast to VO-TPP and VO-DPP.

From the contour plots of the fitted $P(r,a_{iso})$, it appears that for VO-DPP and VO-OEP the meso protons are barely present. This is due to the broad distribution of a_{iso} values for these protons. This manifests in the spectra in the form of broad humps in the range between 0.75 to 1.2 MHz for VO-DPP and 0.5 to 1.25 MHz for VO-OEP and VO-EP. For comparison, the line shape of a meso proton with sharp a_{iso} is shown in Fig. 1a in red. The origin of this distribution is a distribution of ring distortions, which affect the amount of spin density that leaks from the V ion to the meso protons.

Also noticeable in all four cases is non-zero density at slightly negative a_{iso} mostly around.[6] DFT calculations indeed predict negative a_{iso} in this area for some of the aliphatic protons (see Fig. 2). However, VO-TPP only has aromatic protons with a_{iso} very close to zero, which indicates that the experimental spectra do not have sufficient spectral resolution and sensitivity to resolve a_{iso} to less than 0.05 MHz.

VO-OEP and VO-EP show density at $a_{iso} \approx 0$ and $r \approx 9$ Å, even though there are no protons with these parameters in these compounds. This indicates that the resolving power of ENDOR for these long distances is limited. Two reasons for this are that the associated very narrow spectra have very low intensity due to the suppression of intensity close to ν_I in Mims ENDOR, and that every other proton contributes intensity around ν_I as well, leading to spectral congestion. Therefore, the analysis for this region of (r,a_{iso}) is unreliable in these examples.

The fitted distributions make it possible to determine the relative abundance of the various types of protons. For this, specific areas of P_{fit} attributed to each proton type are integrated. The integration areas are based on the 0.05 contour line of $\tilde{P}$ and are shown in Fig. 7a using the contour plot of VO-DPP as an example. Probability mass outside of these areas is designated as unassigned.

The results of this analysis for all compounds are shown in Fig. 7b. Expected values from the Lewis structures are shown in

the upper bar, and integrated intensities obtained from P_{fit} in the lower bar. Overall, the relative intensities are recovered well, particularly for the pyrrole and substituent protons. About 5–10% of intensity results unassigned. Meso protons are underestimated most in VO-DPP, where a small fraction is attributed to coordinated protons. Even though the samples did not contain an axial ligand, Fig. 6b shows small values for the area around 4.5 Å. This is due to the fact that protons from axial ligands and the *ortho* protons from DPP have similar r, as discussed in Section 3.

7 Three-dimensional distributions

It is straightforward to extend the approach introduced in this work to situations where the hyperfine tensors can have significant rhombicity η. This requires a three-dimensional hyperfine parameter distribution $P(r,a_{iso},\eta)$, discretized over a 3D grid such that $P_i = P(r_i,a_{iso,i},\eta_i)$, and an associated three-dimensional prior, $\tilde{P}(r,a_{iso},\eta)$. To demonstrate this, we analyzed VO-EP with a three-dimensional prior, constructed in the same fashion as the 2D prior from the same DFT calculation, but without neglecting η. To avoid an explosion of the number of basis functions, it was necessary to halve the kernel resolution along r and a_{iso}.

Fig. 8a shows the fit to the spectrum. To visualize $P(r,a_{iso},\eta)$, its projections along η, a_{iso}, and r are shown in Fig. 8b, c, and d, respectively. The projection along η produces a two-dimensional distribution $P(r,a_{iso})$ that matches the results from the two-dimensional prior (Fig. 6d) very well. This indicates that the choice of a two-dimensional prior was justified. Analysis of the spectra with the three-dimensional prior yields similar results and in all cases the relative integrals ratios are roughly the same as in the two-dimensional case (data not shown). One significant challenge when going from the 2D to the 3D model is the much larger number of basis functions required in the kernel, resulting in computations with significantly larger memory requirements and slower performance.
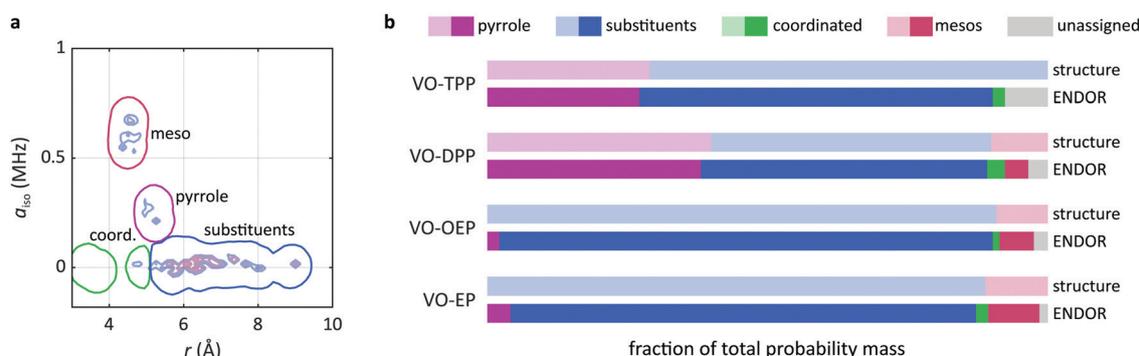

Fig. 7 Ligand proton quantitation. (a) Integration areas that were used to calculate the relative abundances of the proton types. For better illustration, the contour plot of P_{fit} for VO-EP is shown as well. (b) Relative proton abundances for each compound. The upper bar for each compound shows the expected stoichiometric ratios, obtained from the Lewis structure, and the lower bar shows the ones obtained from integration of the fitted hyperfine parameter distribution.
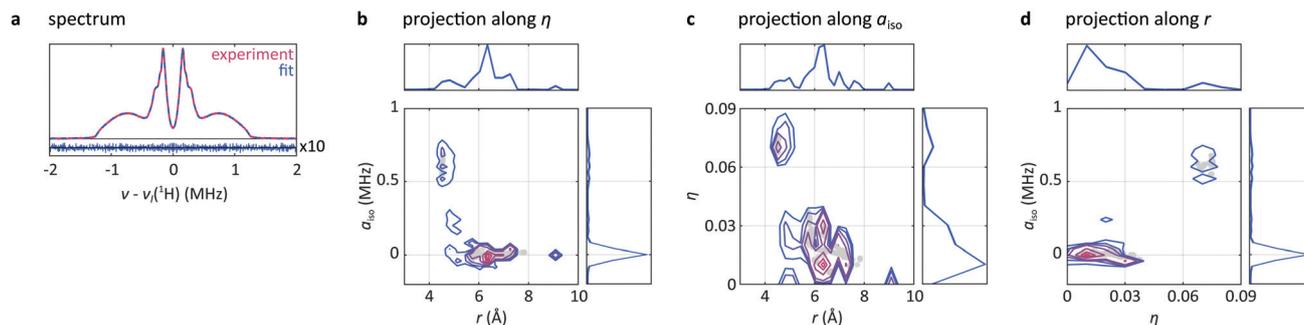
Fig. 8 Analysis of the ENDOR spectrum of VO-EP using a three-dimensional distribution over r, a_{iso}, and the rhombicity parameter η. Shown in (a) is the spectrum (red) and the fit (blue) to it, including the residuals. The projection of the fitted three-dimensional distribution $P(r,a_{iso},\eta)$ along η is displayed in (b). Panels (c) and (d) show the integrals of $P(r,a_{iso},\eta)$ along a_{iso} and r, respectively. Contour levels are drawn at 0.02, 0.05, 0.1, 0.2, 0.5, 0.75, and 0.9 of the maximum of the distribution. The DFT results for protons in VO-EP are shown as gray circles. The regularization parameter α_P was determined *via* the AIC method, and 7440 basis functions were used.

8 Discussion and conclusions

In this work we demonstrated a novel approach to qualitatively and quantitatively analyze ENDOR spectra that uses a model based on a two-dimensional hyperfine parameter distribution. We showed that smoothness regularization fails at recovering the correct target distributions. To overcome this, we regularized the problem with a term that penalizes dissimilarity to a prior distribution based on DFT calculations. We demonstrated the method with four model vanadyl porphyrin molecules. The fitted distance *vs.* contact coupling distributions quantitatively reproduce the spectra and are in good agreement with the physical expectations based on DFT predictions. We also showed that the approach can be extended to extract three-dimensional distributions of distances, contact couplings, and rhombicities. Although demonstrated here for Mims ENDOR only, this method can be applied to other ENDOR experiments (Davies, continuous-wave), as long as the ENDOR line shape for a given hyperfine coupling can be accurately modelled.

The problem discussed here shares the same physical basis as DEER spectroscopy, but several key differences relevant to the analysis exist: (1) in most systems investigated by DEER, contact couplings (exchange couplings) are negligible. This is not the case in ENDOR. Therefore, ENDOR requires a two-dimensional distribution $P(r,a_{iso})$, whereas DEER needs only $P(r)$. (2) In DEER, typically only one other electron spin is significantly coupled to the probed electron spin, whereas in ENDOR there can be many coupled protons. This can lead to significant spectral overlap in ENDOR and aggravates the inversion problem. (3) Whereas in DEER, the dipolar coupling can be distributed due to flexibility of spin labels, in ENDOR it is more often the isotropic coupling that is distributed as a result of structural variability.

We expect distance *vs.* contact coupling distributions to facilitate analysis and interpretation of ENDOR spectra particularly in difficult cases with significant spectral overlap due to many nuclei in the same distance range and with appreciable hyperfine parameter distributions for some nuclei. One particular application could be the speciation of vanadyl petroporphyrins in crude oil.[38–41] However, this ENDOR analysis

method is applicable to other families of paramagnetic compounds for which DFT calculations can be obtained or where additional information is available that allows the generation of a non-flat prior distribution $\tilde{P}$. The structure-based prior can be extended to include published and validated spectroscopic data from the class of compounds under investigation.

Given that the results show distributions for a_{iso}, in particular for the meso protons of VO-DPP, VO-OEP, and VO-EP, it would be reasonable to include an additional smoothing term for a_{iso} in the objective function. Even though we were able to obtain somewhat smoother results by combining the structure-based regularization with smoothness regularization along a_{iso} and r, in our opinion the benefits are outweighed by the fact that values for one (for smoothing only a_{iso}) or two (smoothing for r and a_{iso}) additional hyperparameters need to be selected. Methods for determination of multiple regularization parameters in a generalized *L*-curve framework exist,[42] but it is unclear what the best procedure for regularization parameter selection would be.

As presented, the approach does not allow the determination of the absolute number of protons contributing to the spectrum. To achieve this, the ENDOR amplitude needs to be calibrated, for example *via* an internal standard. Quantification will be more difficult for protons with small a_{iso} and large r, since the associated narrow ENDOR spectra are very weak due to the suppression hole at $\nu \approx \nu_I$.

This approach can also be used for orientation-selective ENDOR spectra, or for a set of orientation-selective ENDOR spectra acquired as a function of magnetic field, by utilizing an appropriate kernel K that includes basis functions from a higher-dimensional hyperfine parameter space.

The signal-to-noise ratio plays an important role in the analysis. The structure-based regularization is fairly stable with respect to more elevated noise levels. However, the method starts fitting the noise if the noise is very strong. This will result in spikier distributions.

The structure-based regularization discussed here requires additional knowledge in the form of DFT simulations based on known structures. If the structure of the spin center is

unknown, then the approach with $\tilde{P}$ still can be used by constructing it such that it represents less specific prior knowledge, for example that it is unlikely to observe a large a_{iso} for long r.

In conclusion, the approach presented here makes congested ENDOR spectra more analyzable, in particular for longer electron–nucleus distances where spectral crowding is typical. However, care must be exercised not to over-interpret the results.

9 Materials and methods

Samples

All model vanadyl complexes were purchased from Frontier Scientific. The deuterated solvents were obtained from Cambridge Isotope Laboratories. Samples were prepared with ≈ 1 mM concentration in $1:1$ (v/v) toluene-d_8/CDCl$_3$, filled into 4 mm o.d. quartz tubes and flash-frozen by immersion into liquid nitrogen.

ENDOR

ENDOR spectra were measured at X-band on a Bruker EleXsys E580 spectrometer with an MD4 probe. For the ENDOR measurements, the magnetic field was set to about 340 mT, so that the microwave was resonant with the $m_S = -1/2 \leftrightarrow +1/2$ transition of VO^{2+}. The resonance frequency of this transition is essentially orientation-independent and therefore excludes orientation selection effects.[41] The temperature was 41–44 K. The Mims ENDOR pulse sequence was used with microwave $\pi/2$ pulses of 10 ns. The radio frequency pulse length was 30 μs, to assure narrow-band excitation of the nuclear transitions and prevent power broadening in the ENDOR spectra. We set $\tau = 150$ ns, which puts the first set of suppression points ("blind spots") with $n = \pm 1$ at ± 3.3 MHz, outside the spectral range of interest. Before analysis, all spectra were phase corrected, symmetrized, and the amplitude normalized to 1. All measured spectra are provided in the ESI.†

DFT

DFT calculations were carried out using ORCA 4.1.1.[43,44] The B3LYP[45–49] functional was used with the EPR-II[50] basis set on all atoms except the vanadium which was modeled with the CP-PPP[51] basis set. The integration grid of size 4 was used throughout.

Data analysis

All data analysis scripts were written in MATLAB and are available in the ESI.† ENDOR basis functions were computed using EasySpin 6[52] for a 47×61 grid (2867 points) with r ranging from 3 to 9.9 Å with a 0.15 Å step size and a_{iso} ranging from -0.2 to 1 MHz with a 0.02 MHz step size, and a convolutional Gaussian broadening with a full width at half maximum (FWHM) of 30 kHz. The resolution of the kernel was chosen to be high enough to avoid artifacts when fitting a spectrum generated with r, a_{iso} values that fall between two grid points. Suppression envelopes were added according to the experimental

parameters. For modeling the matrix peaks, we used a Lorentzian with width $\delta = 0.32$ MHz as per eqn (7). For regularization parameter selection, we used the AIC method.[25,34] It compares solutions with different regularization parameters by comparing relative amounts of information lost for each and selects the one that retains the most information. The relative abundances of the various proton types were calculated via integration of the fitted distribution P_{fit} over regions where the prior distribution for that proton had a value of ≥ 0.05 (see Fig. 7a).

Construction of $\tilde{P}$. We construct $\tilde{P}$ as

$$\tilde{P}(r, a_{\mathrm{iso}}) = \max_{i=1}^{n} G_i(r, a_{\mathrm{iso}}) \qquad (15)$$

where $G_i(r, a_{\mathrm{iso}})$ is a bi-variate unnormalized Gaussian

$$G_i(r, a_{\mathrm{iso}}) = \exp\left(-\frac{(r - r_{0,i})^2}{2\sigma_r^2} - \frac{(a_{\mathrm{iso}} - a_{0,i})^2}{2\sigma_{a_0}^2}\right) \qquad (16)$$

where $r_{0,i}$ is the distance (based on the dipolar coupling) and $a_{0,i}$ the contact hyperfine coupling for proton i. Both values are taken directly from the DFT calculations. The widths σ_r and σ_{a_0} account for uncertainties in the structure and in the DFT calculations. We used values $\sigma_r = 0.2$ Å and $\sigma_{a_0} = 0.04$ Å.

When choosing the width of the Gaussians it is important to choose them large enough to accommodate for uncertainty of the DFT simulations. If the width is chosen too small the method will provide narrow, potentially spiky distributions, and possibly a bad fit. In contrast, if widths for construction of $\tilde{P}$ are chosen too wide, the penalty for unphysical parameter combinations will be too weak and the method will run into similar issues as with least-squares fitting and smoothness regularization.

In eqn (15) we use max instead of a sum for two reasons. First, it allows functions $G_i(r, a_{\mathrm{iso}})$ to be placed close to each other without creating unrealistic ridges, e.g. a ridge between the meso and pyrrole protons in Fig. 5. Second, the amplitudes for all $G_i(r, a_{\mathrm{iso}})$ can be set to one, to avoid artificially increasing bias for areas that have a higher density of DFT predictions, such as the region of the aliphatic and aromatic substituents. Other ways of constructing $\tilde{P}$ are possible; they are all valid as long they represent the DFT predictions (or any other prior information) acceptably.

For construction of the three-dimensional prior $\tilde{P}(r, a_{\mathrm{iso}}, \eta)$ we used a $24 \times 31 \times 10$ grid (7440 points) with r ranging from 3 to 9.9 Å with a 0.3 Å step size, a_{iso} ranging from -0.2 to 1 MHz with a 0.04 MHz step size, and η ranging from 0 to 0.09 with a 0.01 step size. The prior was constructed in a similar fashion as the two-dimensional one, using tri-variate Gaussians that include the results for η from the DFT calculations. For the width along the η dimension we used $\sigma_\eta = 0.0025$.

Conflicts of interest

There are no conflicts to declare.

8334 | *Phys. Chem. Chem. Phys.*, 2021, **23**, 8326–8335

This journal is © the Owner Societies 2021

Acknowledgements

Notes and references

1 G. Feher, *Phys. Rev.*, 1956, **103**, 834–835.

2 J. S. Hyde and A. H. Maki, *J. Chem. Phys.*, 1964, **40**, 3117–3118.

3 J. S. Hyde, *J. Chem. Phys.*, 1965, **43**, 1806–1818.

4 J. R. Harmer, *eMagRes*, John Wiley & Sons, Ltd, Chichester, UK, 2016, pp. 1493–1514.

5 E. R. Davies, *Phys. Lett. A*, 1974, **47**, 1–2.

6 W. B. Mims, *Proc. R. Soc. London, Ser. A*, 1965, **283**, 452–457.

7 T. U. Nick, W. Lee, S. Koßmann, F. Neese, J. Stubbe and M. Bennati, *J. Am. Chem. Soc.*, 2015, **137**, 289–298.

8 G. Rao, L. Tao, D. L. M. Suess and R. D. Britt, *Nat. Chem.*, 2018, **10**, 555–560.

9 G. Rao, L. Tao and R. David Britt, *Chem. Sci.*, 2020, **11**, 1241–1247.

10 C. P. Scholes, A. Lapidot, R. Mascarenhas, T. Inubushi, R. A. Isaacson and G. Feher, *J. Am. Chem. Soc.*, 1982, **104**, 2724–2735.

11 J. Harmer, S. Van Doorslaer, I. Gromov, M. Bröring, G. Jeschke and A. Schweiger, *J. Phys. Chem. B*, 2002, **106**, 2801–2811.

12 D. Baute and D. Goldfarb, *J. Phys. Chem. A*, 2005, **109**, 7865–7871.

13 M. D. Peeks, C. E. Tait, P. Neuhaus, G. M. Fischer, M. Hoffmann, R. Haver, A. Cnossen, J. R. Harmer, C. R. Timmel and H. L. Anderson, *J. Am. Chem. Soc.*, 2017, **139**, 10461–10471.

14 G. T. Babcock, M. K. El-Deeb, P. O. Sandusky, M. M. Whittaker and J. W. Whittaker, *J. Am. Chem. Soc.*, 1992, **114**, 3727–3734.

15 H.-I. Lee, A. F. Dexter, Y.-C. Fann, F. J. Lakner, L. P. Hager and B. M. Hoffman, *J. Am. Chem. Soc.*, 1997, **119**, 4059–4069.

16 T. C. Yang, M. D. Wolfe, M. B. Neibergall, Y. Mekmouche, J. D. Lipscomb and B. M. Hoffman, *J. Am. Chem. Soc.*, 2003, **125**, 7056–7066.

17 M. Brecht, M. van Gastel, T. Buhrke, B. Friedrich and W. Lubitz, *J. Am. Chem. Soc.*, 2003, **125**, 13075–13083.

18 M. Horitani, A. R. Offenbacher, C. A. M. Carr, T. Yu, V. Hoeke, G. E. Cutsail, S. Hammes-Schiffer, J. P. Klinman and B. M. Hoffman, *J. Am. Chem. Soc.*, 2017, **139**, 1984–1997.

19 V. Hoeke, L. Tociu, D. A. Case, L. C. Seefeldt, S. Raugei and B. M. Hoffman, *J. Am. Chem. Soc.*, 2019, **141**, 11984–11996.

20 A. Meyer, S. Dechert, S. Dey, C. Höbartner and M. Bennati, *Angew. Chem., Int. Ed.*, 2020, **59**, 373–379.

21 A. N. Tikhonov, *Dokl. Akad. Nauk*, 1963, **151**, 501–504.

22 M. K. Bowman, A. G. Maryasov, N. Kim and V. J. DeRose, *Appl. Magn. Reson.*, 2004, **26**, 23.

23 G. Jeschke, G. Panek, A. Godt, A. Bender and H. Paulsen, *Appl. Magn. Reson.*, 2004, **26**, 223–244.

24 Y.-W. Chiang, P. P. Borbat and J. H. Freed, *J. Magn. Reson.*, 2005, **172**, 279–295.

25 L. Fábregas Ibáñez, G. Jeschke and S. Stoll, *Magn. Reson.*, 2020, **1**, 209–224.

26 M. Iwasaki, *J. Magn. Reson.*, 1969, **1974**(16), 417–423.

27 S. G. Karshenboim, *Phys. Rep.*, 2005, **422**, 1–63.

28 A. Schweiger and G. Jeschke, *Principles of Pulse Electron Paramagnetic Resonance*, Oxford University Press, Oxford, UK, New York, 2002.

29 P. E. Doan, N. S. Lees, M. Shanmugam and B. M. Hoffman, *Appl. Magn. Reson.*, 2009, **37**, 763.

30 S. A. Dikanov, Y. D. Tsvetkov and A. V. Astashkin, *Chem. Phys. Lett.*, 1982, **91**, 515–519.

31 A. V. Astashkin and A. Kawamori, *J. Magn. Reson.*, 1998, **135**, 406–417.

32 D. R. Kattnig, J. Reichenwallner and D. Hinderberger, *J. Phys. Chem. B*, 2013, **117**, 16542–16557.

33 T. H. Edwards and S. Stoll, *J. Magn. Reson.*, 2018, **288**, 58–68.

34 H. Akaike, *IEEE Trans. Autom. Control*, 1974, **19**, 716–723.

35 C. E. Shannon, *Bell Syst. Tech. J.*, 1948, **27**, 379–423.

36 I. J. Good, *Proceedings of the IEE – Part C: Monographs*, 1956, vol. 103, pp. 200–204.

37 S. Kullback and R. A. Leibler, *Ann. Math. Stat.*, 1951, **22**, 79–86.

38 J. Goulon, A. Retournard, P. Friant, C. Goulon-Ginet, C. Berthe, J.-F. Muller, J.-L. Poncet, R. Guilard, J.-C. Escalier and B. Neff, *J. Chem. Soc., Dalton Trans.*, 1984, **0**, 1095–1103.

39 K. Qian, A. S. Mennito, K. E. Edwards and D. T. Ferrughelli, *Rapid Commun. Mass Spectrom.*, 2008, **22**, 2153–2160.

40 A. M. McKenna, J. M. Purcell, R. P. Rodgers and A. G. Marshall, *Energy Fuels*, 2009, **23**, 2122–2128.

41 D. Mannikko and S. Stoll, *Energy Fuels*, 2019, **33**, 4237–4243.

42 M. Belge, M. E. Kilmer and E. L. Miller, *Inverse Probl.*, 2002, **18**, 1161–1183.

43 F. Neese, *Wiley Interdiscip. Rev.: Comput. Mol. Sci.*, 2012, **2**, 73–78.

44 F. Neese, *Wiley Interdiscip. Rev.: Comput. Mol. Sci.*, 2018, **8**, e1327.

45 A. D. Becke, *Phys. Rev. A: At., Mol., Opt. Phys.*, 1988, **38**, 3098–3100.

46 P. J. Stephens, F. J. Devlin, C. F. Chabalowski and M. J. Frisch, *J. Phys. Chem.*, 1994, **98**, 11623–11627.

47 C. Lee, W. Yang and R. G. Parr, *Phys. Rev. B: Condens. Matter Mater. Phys.*, 1988, **37**, 785–789.

48 A. D. Becke, *J. Chem. Phys.*, 1993, **98**, 5648–5652.

49 A. D. Becke, *J. Chem. Phys.*, 1993, **98**, 1372–1377.

50 N. Rega, M. Cossi and V. Barone, *J. Chem. Phys.*, 1996, **105**, 11060–11067.

51 F. Neese, *Inorg. Chim. Acta*, 2002, **337**, 181–192.

52 S. Stoll and A. Schweiger, *J. Magn. Reson.*, 2006, **178**, 42–55.

This journal is © the Owner Societies 2021

Phys. Chem. Chem. Phys., 2021, **23**, 8326–8335 | **8335**